



# Simulation and modal analysis of transonic shock buffets on a NACA-0012 airfoil

Andre Weiner\* and Richard Semaan.†

*Technische Universität Braunschweig, Institute of Fluid Mechanics, Braunschweig, 38108, Germany*

**We perform 2D and 3D simulations of a NACA-0012 airfoil at pre- and post-buffet onset employing an IDDES simulation approach with Spalart-Allmaras closure model. The 3D simulations provide more realistic results in terms of buffet frequency and shock motion, highlighting the need for three-dimensional and scale-resolving simulations to properly capture the flow physics of the transonic buffet phenomenon. Dynamic mode decomposition identifies flow structures in the shock, boundary layer, and wake region that are slaved by the buffet cycle. We provide a fully reproducible, fully open-source simulation workflow to investigate transonic shock buffets. The workflow includes tools for visualization and modal analysis.**

## Nomenclature

$a$	=	local speed of sound
$a_\infty$	=	freestream speed of sound
$\mathbf{A}$	=	discrete linear operator
$\mathcal{A}$	=	continuous linear operator
$\tilde{\mathbf{A}}$	=	reduced discrete linear operator
$\mathbf{b}$	=	DMD mode amplitudes
$c$	=	chord length
$c_l$	=	lift coefficient
$c_p$	=	pressure coefficient
DES	=	Detached Eddy Simulation
DDES	=	Delayed DES
DMD	=	Dynamic Mode Decomposition
$f$	=	frequency
$\tilde{f}$	=	normalized frequency $2\pi c f / U_\infty$
IDDES	=	Improved DDES
LES	=	Large Eddy Simulation
$Ma$	=	local Mach number
$Ma_\infty$	=	freestream Mach number
$N_{cells}$	=	number of control volumes
$r$	=	matrix rank
RANS	=	Reynolds Averaged Navier Stokes
$Re_\infty$	=	freestream Reynolds number
SA	=	Spalart-Allmaras
SST	=	Shear Stress Transport
SVD	=	Singular Value Decomposition
$t$	=	time
$\tilde{t}$	=	normalized time $ta_\infty/c$
$\mathbf{u}$	=	velocity vector $\mathbf{u} = [u, v, w]^T$
$\mathbf{U}$	=	left singular vectors
$U_\infty$	=	freestream velocity
URANS	=	Unsteady RANS
$\mathbf{V}$	=	right singular vectors

\*Post-doctoral researcher, flow modeling and control group, a.weiner@tu-braunschweig.de

†Group leader, flow modeling and control group, r.semaan@tu-braunschweig.de

$\mathbf{W}$	=	eigenvectors of $\tilde{\mathbf{A}}$
WMLES	=	Wall Modeled LES
$\tilde{x}$	=	$x$ -coordinate divided by chord length
$\tilde{x}_s$	=	shock position divided by chord length
$\mathbf{x}_n$	=	snapshot of state vector at time step $n$
$\mathbf{X}$	=	data matrix of snapshots
$\mathbf{X}'$	=	data matrix shifted by one snapshot
$\tilde{y}$	=	$y$ -coordinate divided by chord length
$y^+$	=	normalized coordinate normal to surface
$\alpha$	=	angle of attack
$\gamma$	=	heat capacity ratio
$\Lambda$	=	eigenvalues of $\mathbf{A}$
$\Sigma$	=	singular values
$\nu$	=	kinematic viscosity
$\Phi$	=	DMD modes, eigenvectors of $\mathbf{A}$
$\Omega$	=	eigenvalues of $\mathcal{A}$

## I. Introduction

THE transonic shock buffet is a flow phenomenon characterized by self-sustained oscillations caused by interactions between the shock wave and the boundary layer over an airfoil in transonic flow conditions. Numerous experimental and numerical studies have been conducted to deepen our understanding of the buffet mechanism and enable predictions of its onset. In the following, we briefly review some numerical works concerned with buffet over two-dimensional airfoils. For a recent and comprehensive overview, we refer the reader to Giannelis et al. [1].

Earnest numerical investigations of two-dimensional transonic buffet can be traced to the late 1990s and early 2000s. Frequently employed airfoils are the Onera OAT15 [2–10] and the RA16SC1 [11–13], presumably due to the availability of experimental validation data. Other investigated airfoils are the NACA-0012 [12], the NACA-64A204 [10, 12], and the BKG no.1 [14]. Due to the high Reynolds numbers  $Re = cU_\infty/\nu$  in the range  $3 \times 10^6 \leq Re \leq 20 \times 10^6$ , most studies employ URANS simulations. The most frequently employed RANS closure models are Spalart-Allmaras (SA) and  $k-\omega$ -SST. Both appear to be capable to predicting the self-sustained buffet cycles at the correct angle of attack with the correct frequency *if* the model constants are calibrated to the transonic flow conditions.

An increasing number of scale-resolving simulations are being conducted. Deck et al. [3] were likely the first to employ a zonal DES (ZDES) approach. Fukushima et al. [9] provide a comparison of ZDES, delayed DES (DDES), improved DDES (IDDES), and wall-modeled LES (WMLES) results obtained for the OAT15 profile.

For both URANS and scale-resolving simulations, the influence of the discretization scheme has also been investigated [2]. However, thanks to improvements in numerical methods over the past two decades as well as the ability to employ much denser meshes, the spatial discretization has become a minor concern. Nonetheless, care has to be taken when creating unstructured meshes. For example, Illi et al. [15] use block-structured meshes as well as hybrid meshes with block-structured cell layers about the airfoil and triangular cells in the remaining domain. They show how the buffet can be triggered by numerical instabilities originating from triangular cells close to the airfoil's surface. Of course, such a dependency on the mesh topology is highly undesirable.

Despite the respectable number of available literature, it remains difficult to draw definite conclusions as to what simulation strategy is favorable and what predictive quality to expect from the simulations. This difficulty mainly arises because the reported results are sometimes contradictory, as are outlined in the following:

- **buffet onset:** many studies report on URANS simulations that do not exhibit oscillations and converge to a steady solution at the experimentally identified buffet onset angle of attack, e.g. [2, 3, 5, 11, 12], whereas others report buffet onset at the correct angle of attack while employing the same turbulence closure [4, 8, 10, 13, 14]. Possible sources for this discrepancy are the strong dependency on model constants, as reported in [8, 11], and differences in the implementation details like model extensions, which are missing or incomplete in the published manuscripts. Concerning the hybrid RANS-LES approaches, ZDES, DDES, IDDES, and WMLES all seem capable of predicting the correct onset angle of attack. However, also for the hybrid approaches the RANS closure model constants have neither been properly reported nor have their influence been investigated.
- **shock position:** URANS simulations tend to predict the mean shock position too far downstream both at pre-onset and onset conditions [2, 3, 5, 7, 12], while some hybrid approaches (ZDES and IDDES) predict the shock too far

upstream [3, 6], at least for the OAT15 profile. The downstream position of the shock might be related to the increased observed buffet onset angle. Again it appears that modified model constants may be used to move the shock position [8].

- **buffet frequency:** experiments [3, 16] show that the dominant buffet frequency, typically in the 30 – 100Hz range, strongly depends on both angle of attack  $\alpha$  and Mach number  $Ma_\infty = U_\infty/a_\infty$ . Inside the buffet envelop, an increase of  $\alpha$  or  $Ma_\infty$  yields an increased buffet frequency. While tweaking the model constants may help to fit the experimental data for one flow condition, the sensitivity of the buffet frequency to the flow conditions is typically not correctly predicted by URANS simulations [8, 13]. Therefore, it is not too surprising that the numerically predicted buffet frequency is sometimes too low [11, 12, 14] or too high [2, 4, 5, 10]. For the hybrid approaches, the results are also mixed. While in references [3, 9] a good agreement with the experimentally obtained spectrum is reported (ZDES, WMLES), DDES and IDDES-based studies [5, 6] overestimate the buffet frequency by about ten percent. It has to be noted that for the hybrid approaches fewer results concerning the numerical sensitivity to  $Ma_\infty$  and  $\alpha$  variations are available.
- **lift coefficient:** the predicted mean and amplitude of the oscillating lift coefficient are closely related to the shock position and the shock motion during a buffet cycle. Grossi et al. [5] compare two-dimensional URANS and three-dimensional DDES simulations of an OAT15 profile at buffet conditions. The 2D simulations display a larger mean lift value and also larger amplitudes compared to the 3D simulations. The authors attribute this behavior to the shock position, which is predicted too far downstream for the URANS models. These observations are also representative for other URANS investigations.

Besides the previous challenges, another main difficulty in assessing previous studies is the unavailability of the source code, the full data, and a detailed description. In this study, we aim to simplify numerical investigations of shock buffets by providing a fully reproducible and open-source simulation workflow including the simulation setup as well as consecutive analysis and post-processing steps. The workflow may still have space for improvements but hopefully provides a good basis for future studies. The complementary data is available via *Github* [17].

The main post-processing tool we use to analyze the results is dynamic mode decomposition (DMD), which is a data-driven technique for analyzing and modeling dynamical systems [18]. Taira et al. [19] provide a recent overview of DMD and related modal decomposition techniques applied to unsteady fluid flows. In the context of 2D transonic buffets, DMD has been used to analyze URANS data of OAT15 [7, 10], RA16SC1 [13], and NACA-64A [10] profiles. A DMD analysis yields modes, with each mode having a single characteristic frequency of oscillation and growth/decay rate. A more detailed description is provided in section II.B. Expectedly, all previous studies [7, 10, 13] found high amplitudes at the buffet frequency and its harmonics. The corresponding DMD modes are typically dominated by structures around the shock and the separated boundary layer. The growth rates are relatively difficult to interpret because of their sensitivity to small changes in the data. Despite its apparent ease of use, a improper implementation of DMD can yield inaccurate results. One common issue is the utilization of an unsuitable state vector. Previous studies used the velocity fluctuations [7, 10] or the pressure [13], which are adequate choices for incompressible flows, but not necessarily for compressible flows. Moreover, simulations of shock boundary layer interactions naturally employ a high mesh density close to the airfoil and about the shock. Therefore, it is recommended to weigh the snapshot data with the cell volumes to create a more balanced state vector, something previous studies did not consider.

The remainder of this article is structured as follows. In the next section, we describe the simulation setup and establish a theoretical foundation for DMD. Section 2 quantifies the influence of mesh resolution and wall modeling. Thereafter, we compare the results of two- and three-dimensional simulations of transonic buffets and report typical aerodynamic properties like lift and pressure coefficients. Finally, we present the DMD analysis characterizing the buffet phenomenon in our IDDES simulations.

## II. Methodology

### A. Numerical simulations

The simulations are performed using the *OpenFOAM-v2012\** library. Two different numerical solvers were tested, namely the density-based *rhoCentralFoam* and the pressure-based *rhoPimpleFoam* in a preliminary study. In principal, both solvers are able to simulate the self-sustained shock-boundary layer-interaction. However, the pressure-based solver requires a significantly higher mesh resolution to capture the shock and exhibits a larger mesh dependency and small

---

\*<https://www.openfoam.com/>

oscillations around the shock compared to the density-based approach. Therefore, all results presented in this article are generated with the *rhoCentralFoam* solver.

*OpenFOAM* implements a finite volume approach for unstructured meshes with a cell-centered, co-located variable arrangement. Face fluxes are reconstructed based on the two neighboring cell-centered values of each face. *rhoCentralFoam* solves the conservation equations for mass, momentum, and energy by operator splitting [20]. In the predictor step, the convection of conserved quantities, i.e., mass density, momentum density, and energy density, are computed explicitly. In the corrector step for momentum and energy, the diffusive terms are discretized and solved implicitly for the primitive variables, i.e., energy and velocity. The convective transport is computed based on the interpolation scheme by Kurganov, Noelle, and Petrova [21]. To interpolate the cell-centered values of the conserved variables to the faces, van Leer's limiter [22] is employed. Linear interpolation is used for all remaining face interpolations.

The solver supports generic RANS, LES, or hybrid RANS-LES simulations. Attempts to predict transonic buffet with standard SA and  $k-\omega$ -SST RANS models at the critical angle of attack were not successful. We did not attempt to modify model constants or to increase the angle of attack. Instead, we employ hybrid SA-IDDES simulations. The implementation is based on the work by Gritskevich et al. [23].

The airfoil geometry is a simple subsonic NACA-0012 with a blunt trailing edge of height  $2.5 \times 10^3 c$ . The choice is motivated by our desire to use a public domain geometry for which experimental data is available. The computational mesh with the lowest resolution is depicted in figure 1. The block-structured C-type mesh is generated with the *blockMesh* utility. Considering the airfoil's nose as origin, the lower, upper, and upstream boundaries are located at a distance of  $10c$ , where  $c$  denotes the chord length. The downstream boundary is  $30c$  away from the airfoil. For the 3D simulations, a spanwise section of  $0.2c$  width is used, which is  $0.05c$  less than in references [3, 5]. The rectangular elements forming the airfoil's surface are roughly quadratic for the most part. The 2D meshes are identical to their 3D counterparts but have only one cell in the spanwise direction.

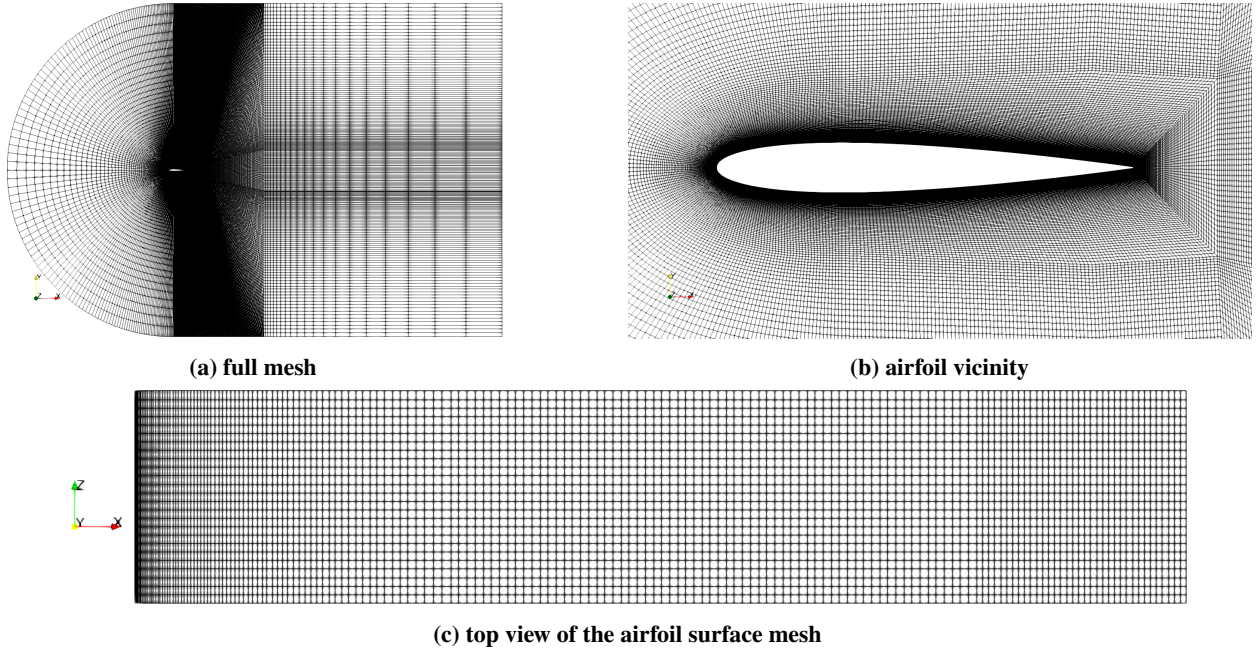


**Fig. 1 Various views of the computational mesh employed in the simulations.**

Since the convective transport step is solved implicitly, the Courant number is limited to  $Co_{max} = 0.25$ . Considering a dimensionless time defined as:

$$\tilde{t} = \frac{ta_{\infty}}{c} = \frac{tU_{\infty}}{cMa_{\infty}}, \quad (1)$$

where  $a_{\infty}$ ,  $U_{\infty}$ , and  $Ma_{\infty}$  are the freestream speed of sound, velocity, and Mach number, respectively, the time step employed in the simulations is  $\Delta \tilde{t}_{sim} \approx 10^{-5}$ . The small timestep is a limitation of the current workflow. Because we perform modal analysis of the flow field, snapshots are saved relatively frequently at intervals of  $\Delta \tilde{t} \approx 5.5 \times 10^{-2}$ .

Results for different mesh resolutions and simulation approaches are presented in section III. For more details on the simulation setups, the reader is referred to the publicly available repository [17].

## B. Dynamic mode decomposition

The main idea behind dynamic mode decomposition is to identify a linear operator  $\mathbf{A}$  that maps snapshots of the state vector  $\mathbf{x}$  by one timestep  $\Delta t$  into the future:

$$\mathbf{X}' := \mathbf{A}\mathbf{X}, \quad (2)$$

or

$$\mathbf{A} := \mathbf{X}'\mathbf{X}^\dagger, \quad (3)$$

where  $\dagger$  denotes the Moore-Penrose inverse matrix operator, and the snapshot matrices  $\mathbf{X}$  and  $\mathbf{X}'$  are defined as:

$$\mathbf{X} = \begin{bmatrix} | & | & & | \\ \mathbf{x}_1 & \mathbf{x}_2 & \dots & \mathbf{x}_{N-1} \\ | & | & & | \end{bmatrix}, \quad \mathbf{X}' = \begin{bmatrix} | & | & & | \\ \mathbf{x}_2 & \mathbf{x}_3 & \dots & \mathbf{x}_N \\ | & | & & | \end{bmatrix}. \quad (4)$$

The snapshots of the state vector are usually recorded at equidistant time intervals. The operator's eigen-decomposition, namely  $\mathbf{A} = \mathbf{\Phi}\mathbf{\Lambda}\mathbf{\Phi}^{-1}$ , has several useful properties. First, it can be used to make future prediction based on the relation [24]:

$$\mathbf{x}_n = \mathbf{\Phi}\mathbf{\Lambda}^n\mathbf{b}, \quad (5)$$

where  $\mathbf{b} = \mathbf{\Phi}^{-1}\mathbf{x}_0$  denotes the so-called mode amplitudes. The columns of  $\mathbf{\Phi}$  are referred to as DMD modes, and they may be ranked according to the corresponding rows in the  $\mathbf{b}$  vector (the mode amplitudes). In the time-continuous space, the problem of advancing a state vector in time is posed as:

$$\frac{d\mathbf{x}}{dt} = \mathcal{A}\mathbf{x}, \quad (6)$$

where  $\mathcal{A}$  is the continuous counterpart of  $\mathbf{A}$ . Both operators are related as,

$$\mathbf{A} = \exp(\mathcal{A}\Delta t), \quad (7)$$

and similarly, the relation between the eigenvalues is:

$$\mathbf{\Lambda} = \exp(\mathbf{\Omega}\Delta t), \quad (8)$$

where  $\mathbf{\Omega}$  are the eigenvalues of  $\mathcal{A}$ . Equation (6) has a relatively simple analytical solution [24]:

$$\mathbf{x}(t) = \mathbf{\Phi}\exp(\mathbf{\Omega}t)\mathbf{b}. \quad (9)$$

Noticing that the eigenvalues  $\omega_i$  in  $\mathbf{\Omega}$  are usually complex numbers, the exponential term may be split up and reformulated using Euler's formula:

$$\exp(\omega_i t) = \exp(\Re(\omega_i)t) [\cos(\Im(\omega_i)t) + j\sin(\Im(\omega_i)t)]. \quad (10)$$

Therefore, the real part of an eigenvalue  $\Re(\omega_i)$  is interpreted as growth rate of mode  $i$ , and the imaginary part  $\Im(\omega_i)$  yields the mode's characteristic frequency  $2\pi f_i = \Im(\omega_i)$ .

In the context of fluid flows, the state vector is typically extremely large such that the eigen-decomposition of  $\mathbf{A}$  has to be approximated. The most widely used procedure invokes a low-rank approximation of  $\mathbf{A}$  by means of a singular value decomposition (SVD) of the first snapshots matrix,  $\mathbf{X} \approx \mathbf{U}_r \mathbf{\Sigma}_r \mathbf{V}_r^H$ , where  $r$  indicates that the matrices are truncated. If  $\mathbf{A}$  has a low rank, then the reduced operator

$$\tilde{\mathbf{A}} = \mathbf{U}_r^H \mathbf{A} \mathbf{U}_r = \mathbf{U}_r^H \mathbf{X}' \mathbf{V}_r \mathbf{\Sigma}_r^{-1} \quad (11)$$

has the same non-zero eigenvalues as  $\mathbf{A}$ . The modes are reconstructed following the formulation suggested by Tu et al. [25] yielding the so-called exact DMD modes:

$$\mathbf{\Phi} = \mathbf{X}' \mathbf{V}_r \mathbf{\Sigma}_r^{-1} \mathbf{W}. \quad (12)$$

Applying DMD to airfoil simulations with transonic buffet entails some peculiarities, which previous studies have did not consider. First, for compressible flow configurations, the velocity  $\mathbf{u} = [u, v, w]^T$  and thermodynamic variables (e.g., density  $\rho$ , pressure  $p$ , enthalpy  $h$ ) are dynamically coupled. Thus, the formulation of a meaningful state vector is less clear than in the incompressible case. Combining different fields in a single state vector is not proper, since pressure, density, and velocity usually have very different orders of magnitude and different units. Rowley et al. [26] suggested a physically-based state vector that includes the velocity components and the stagnation enthalpy  $h$ :

$$h = \frac{2}{\gamma - 1} a, \quad (13)$$

where  $\gamma$  is the heat capacity ratio and  $a$  is the local speed of sound. Specifically, if  $\mathbf{u}_n$ ,  $\mathbf{v}_n$ , and  $\mathbf{w}_n$  are the snapshot velocity components of the velocity vector  $\mathbf{u}$ , and  $\mathbf{a}_n$  is the local speed of sound snapshot, then the state vector at time  $n$  is defined as:

$$\mathbf{x}_n = [\mathbf{u}_n, \mathbf{v}_n, \mathbf{w}_n, 2\mathbf{a}_n/(\gamma - 1)]^T. \quad (14)$$

Another important consideration for DMD concerns the utilization of a weighted inner product. Since the mesh resolution is usually nonuniform, regions with high cell density may wrongly dominate the matrix operations. Therefore, the data matrix entries should be weighted by the cell volumes to give flow structures close to the airfoil and in the wake a more uniform weight. Instead of using the cell volume directly, we use its square root instead. This alternation is rooted in the definition of the left singular vectors  $\mathbf{U}$  by means of inner products. The interested reader is referred to chapter 11.4 in reference [27].

Finally, the modal analyses are performed on a rectangular domain defined by  $-c \leq x \leq 4c$  and  $-c \leq y \leq c$ . For the 3D simulations, a single slice at  $z/c = 0$  is extracted. This domain is large enough to reduce long-term convection effects, which are detrimental to the robustness of the spectral analysis. To compute the DMD, we use the *flowTorch* package [28], which is an open-source Python package tailored to the analysis and modeling of fluid flows.

### III. Results

In the present study, we replicate the experimental flow conditions of McDevitt and Okuno [16]. The Reynolds number based on the free stream velocity  $U_\infty$  is  $Re_\infty = U_\infty c / \nu = 10^7$ , and the free stream Mach number is  $Ma_\infty = U_\infty / a_\infty = 0.75$ . These flow conditions correspond to *set 1* of the experimental study. In particular, we focus on test cases with an angle of attack of  $\alpha = 2^\circ$  and  $\alpha = 4^\circ$ . The former case yields a steady attached flow, whereas the latter case lies in the buffet regime.

#### A. Influence of mesh resolution and wall functions

First, we present the mesh dependency study for  $\alpha = 2^\circ$  and  $\alpha = 4^\circ$ , that we perform on 2D SA-IDDES simulations. Note that 2D hybrid simulation are not necessarily expected to yield physically meaningful results, because of the two-dimensionality of the simulations. Nonetheless, we found this approach useful to test multiple mesh topologies and resolutions. Moreover, the results presented in the next section show that 2D and 3D approaches are qualitatively comparable, at least to some extend.

**Table 1** Parameters of 2D mesh dependency study;  $y^+$  denotes the inner wall normal unit averaged over the airfoil at  $\alpha = 2^\circ$ ;  $N_{cells}$  is the number of control volumes.

	ref. 0	ref. 1	ref. 2
$y^+$	4.82	3.73	3.03
$N_{cells}/10^3$	170	197	223

Table 1 lists the main characteristics of the tested meshes with three refinement levels. Cell refinement is performed only in the wall-normal direction. The number of cells along the chord is kept constant at 240 for both lower and upper side. Figure 2 presents the pressure coefficient distribution for the three investigated meshes along with the reference experimental one at pre-onset conditions  $\alpha = 2^\circ$ . As can be seen in the figure, the different mesh resolutions yield visually indistinguishable results. However, compared to the experimental results, the shock is shifted upstream. It is noteworthy that the pressure coefficient distributions from these 2D SA-IDDES simulations are indistinguishable from SA-based URANS predictions, which are not presented here for brevity. In contrast to our results, Iovnovish et al. [12]

predict the shock position more downstream employing formally the same RANS closure. We also repeated the mesh dependency study with only 175 cells along the chord (about 30% fewer cells), and found identical results.

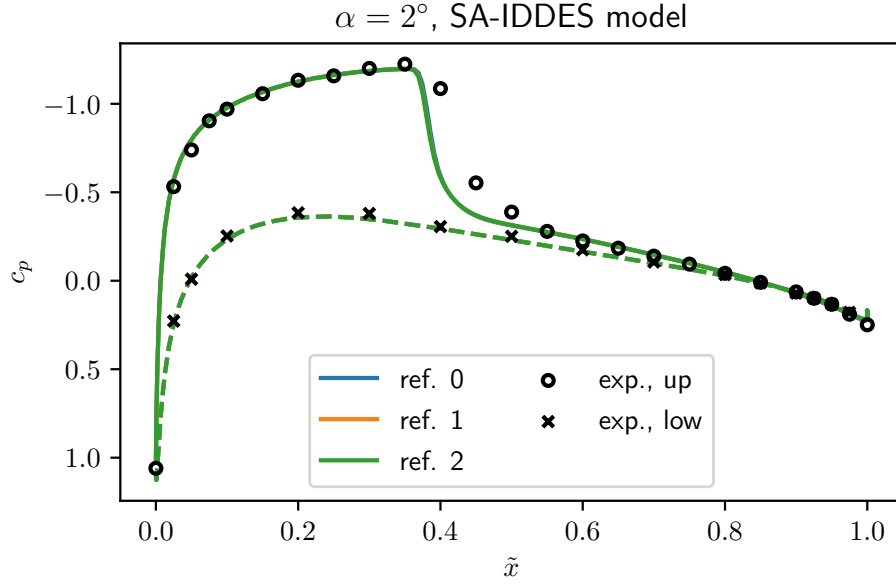


**Fig. 2** Pressure coefficient  $c_p$  at  $\alpha = 2^\circ$  for several mesh resolutions according to table 1.

For the buffet conditions at  $\alpha = 4^\circ$ , no experimental data for the surface pressure are available. Similar to the pre-onset case, the statistical results for the pressure coefficient depicted in figure 3 demonstrate a vanishingly small mesh dependency. The mean pressure coefficients and the standard deviation, depicted as shaded area, are averaged over 2000 snapshots comprising  $\approx 9$  buffet cycles. The elevated fluctuations compared to the  $\alpha = 2^\circ$  case are indicative of the buffet phenomenon, which is expected at these conditions. A further analysis of the pressure coefficients follows in the next section. Regarding the SA-URANS simulations employing the SA baseline model, the results converged to a steady flow state with no oscillations regardless of the mesh resolution.

Wall functions have the potential to accelerate the simulations by allowing for a reduced mesh resolution close to the wall and increased numerical timesteps. Figure 4 shows the pressure coefficient distributions at pre-onset conditions for successively coarsened meshes with and without wall correction based on Spalding's function. As the figure shows, the curves are very similar. Only the shock position shifts slightly in the downstream direction. For buffet conditions, both surface pressure and lift coefficient are qualitatively similar when employing wall functions (not presented here). However, frequency and amplitude of the buffet motion vary slightly with the mesh resolution, which has been also reported previously by Goncalves et al. [11]. Therefore, the results presented in the next section for both 2D and 3D simulations are those obtained without employing wall functions at the lowest resolution level. For completeness, we aim to conduct a dedicated mesh dependency study for the 3D simulations in future investigations.

## B. Lift and pressure coefficients

In this section, we compare the pressure and lift coefficients of 2D and 3D simulations at buffet conditions. Figure 5 shows the mean and standard deviation for the surface pressure coefficient. Only the standard deviation on the suction side is depicted for clarity. Mean and standard deviation are computed based on 2000 samples comprising nine cycles in 2D and 689 samples comprising three cycles for the 3D simulation. Despite the different samples sizes, the 3D data are representative since comparable results are obtained when evaluating only two cycles. The shock motion and mean shock position can be determined by examining the section of high pressure fluctuations in the first half of the airfoil. The mean shock position is about  $\tilde{x}_s = x/c \approx 0.27$  in the 3D and  $\tilde{x}_s \approx 0.3$  in the 2D setup. Moreover, the 2D simulation yields a larger shock motion of  $\Delta\tilde{x}_s \approx 0.29$  compared to  $\Delta\tilde{x}_s \approx 0.19$  in 3D. The 2D shock motion is close to the SA-URANS result reported by Iovnovich et al. [12] for the same airfoil ( $\Delta\tilde{x}_s \approx 0.26$ ). The comparatively smaller 3D shock motion is in agreement with the DDES results for the OAT15 profile presented by Grossi et al. [5]. Shifting the

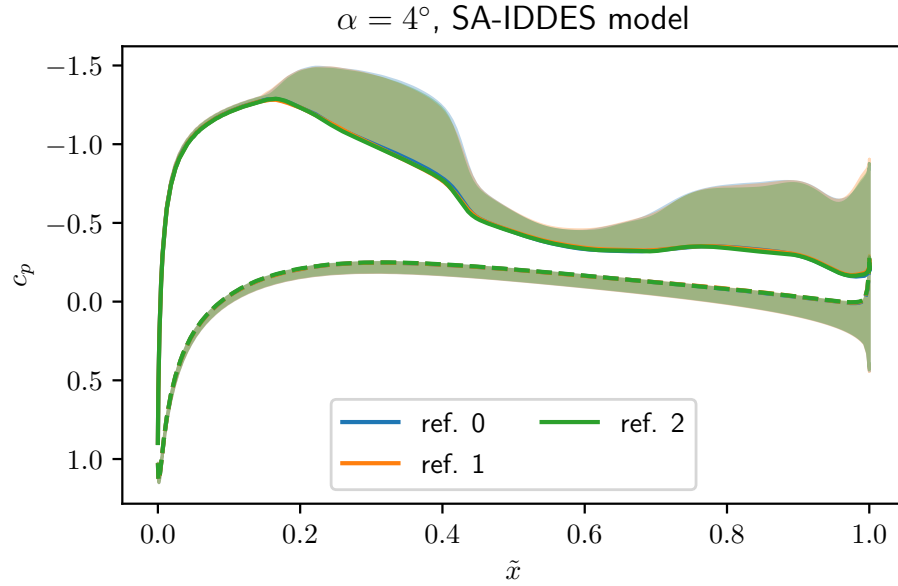


**Fig. 3** Pressure coefficient  $c_p$  at  $\alpha = 4^\circ$  for several mesh resolutions according to table 1; the shaded areas correspond to the standard deviation.

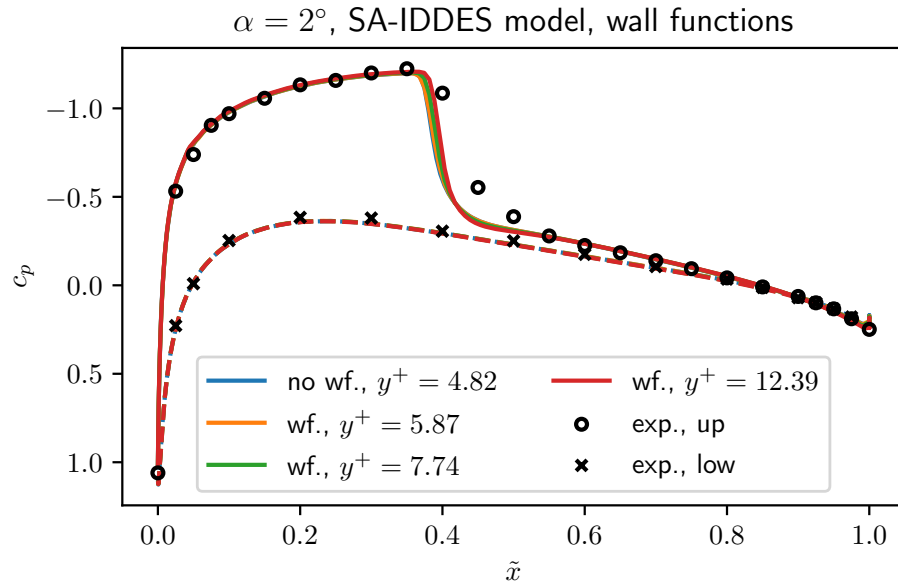


**Fig. 4** Pressure coefficient distributions  $c_p$  at  $\alpha = 2^\circ$  computed on coarsened meshes with and without wall correction based on Spalding's function.

attention towards the trailing edge, the 2D simulations show significantly larger pressure fluctuations. These fluctuations are directly related to the spanwise symmetry imposed in the 2D simulations, as elaborated at the end of this section. Moreover, the 3D boundary layer already separates on average at  $\tilde{x} \approx 0.5$  compared to  $\tilde{x} \approx 0.7$  in 2D.

The lift coefficient sequences presented in figure 6 reflect the same observations as for the surface pressure. Therefore, it comes as no surprise that the mean lift coefficient and the lift amplitude are smaller in the 3D simulations. This observation is shared by other authors [3, 5]. The difference in the mean lift and the lift amplitude between the 2D and 3D simulations amounts to  $\approx 38\%$  and  $\approx 8\%$ , respectively. The lift amplitude is approximately 2.5 times larger than the



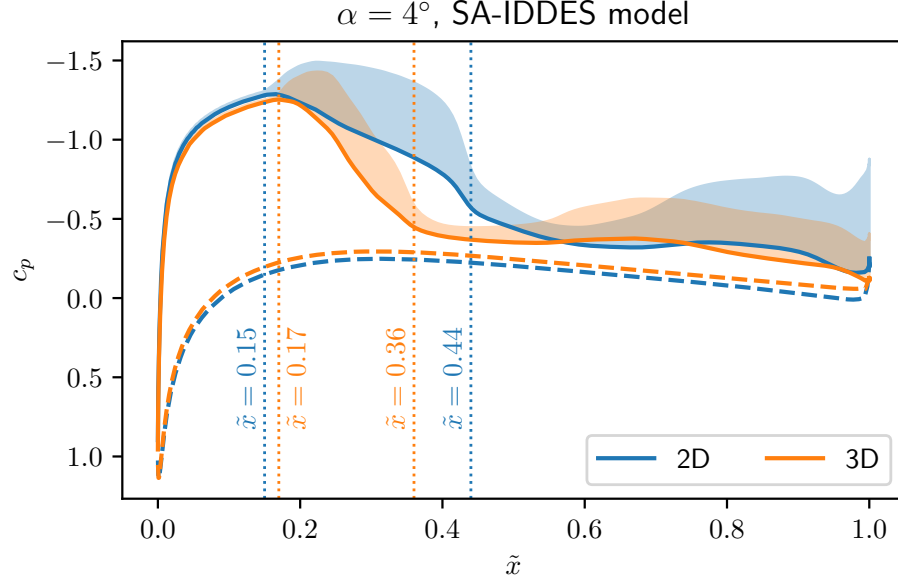


**Fig. 5 Comparison of the pressure coefficient distribution  $c_p$  at  $\alpha = 4^\circ$  between 2D and 3D simulations; the shaded area on the suction side corresponds to one standard deviation.**

value reported by Iovnovich et al. [12]. However, note that URANS yields much smoother lift curves compared to the IDDES simulations. Therefore, it would be more suitable to compare the results based on the standard deviation rather than minimum and maximum values. Another difficulty in conducting direct comparisons is that many studies report result at increased angles of attack. Since both mean lift and amplitude change significantly with  $\alpha$ , a quantitative comparison is less meaningful. Finally, a careful examination of the three buffet cycles depicted in figure 6 reveals that the oscillation cycles are slightly longer for the 3D simulation despite the less pronounced shock motion. This observation is also confirmed quantitatively by the DMD results presented in the next section.

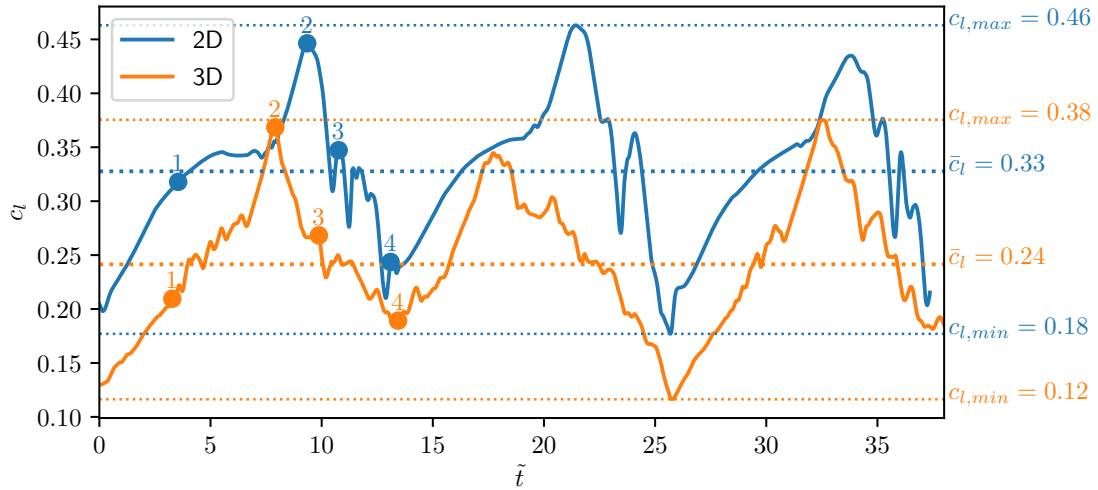


**Fig. 6 Comparison of lift coefficient  $c_l$  at  $\alpha = 4^\circ$  between 2D and 3D simulations.**

Figure 7 visualizes snapshots from the 2D and 3D simulations at comparable phases during one buffet cycle. The snapshot times are also marked in the lift curves in figure 6. Besides the already observed stronger shock motion in 2D, the following points may be noted:

- the supersonic region is significantly larger in the 2D simulations
- the boundary layer separation and the subsequent vortex shedding in the 3D simulations never ceases, which is in contrast to the 2D simulations; refer to the snapshots in the first row of figure 7
- the boundary layer separation in 2D is much stronger than in 3D; the supersonic region above the trailing edge is mostly absent in the 3D simulations; the strong separation is introduced by the enforced symmetry in spanwise direction and causes strong pressure fluctuations close to the trailing edge
- the 2D vortex shedding is significantly stronger (higher local velocities, larger vortices) than in 3D

### C. Dynamic mode decomposition

DMD is a powerful tool to extract coherent, frequency-separated flow structures from complex flow data. However, the spectral decomposition is susceptible to small changes in the data and in the algorithm settings. Besides the already mentioned composition of the state vector and the weighting with the cell volume, the sampling frequency, the overall length of the sequence, and the SVD truncation are also important. Compared to previous studies [7, 10, 13], the present data contains more resolved turbulence and thus higher temporal and spatial variance in all fields. While references [7, 13] suggest  $N \approx 100$  snapshots per cycle to be sufficient, our results degenerated when using less than  $N \approx 200$  snapshots per cycle. Moreover, the SA-IDDES cycles are much more irregular, especially in the 3D simulation. Therefore, applying DMD to a single cycle (as performed in [13]) would yield different outcomes depending on the cycle. From our investigations, we observe that the overall number of cycles is less critical than the number of snapshots per cycle.

Figure 8 compares the DMD mode spectra obtained from the 2D and 3D simulations. To better isolate the relevant modes, we truncated the SVD at  $r = 50$  for the 3D data and  $r = 100$  for the 2D data. The present results are relatively robust to the rank truncation. Reducing  $r$  further removes modes associated with higher frequencies, but leaves the identified lower frequencies unaltered. Both DMD analyses clearly identify a dominant mode associated with the buffet frequency. Table 2 lists the identified buffet frequencies, as well as those from the literature. The buffet frequency for the 2D and 3D simulation are 25% and 42% larger than the experimentally determined one in [16]. It should be noted that for the 3D data the buffet cycles are much less regular than in the 2D or URANS simulations. Therefore, the sequence length employed in the 3D data is not yet sufficient to draw definite conclusions. We expect a closer convergence to the experimental value as more data become available.

Besides the buffet mode, the 3D spectrum shows harmonics at twice and four times the buffet frequency. Another interesting peak appears between 800Hz and 900Hz ( $11.8 < \bar{f} < 13.3$ ). The latter frequency is associated with the vortex shedding at the trailing edge, as will be shown at the end of this section. The 2D spectrum has a similar structure, but the amplitudes of frequencies larger than roughly 500Hz ( $\bar{f} > 7.4$ ) are more pronounced than in the 3D data. These peaks are presumably caused by the strong boundary layer separation and vortex shedding, which is also visible in figure 7.

**Table 2** Dimensionless shock buffet frequency  $\bar{f} = 2\pi c f / U_\infty$ .

experiment [16]	Iovnovich et al. [12]	SA-IDDES, 2D	SA-IDDES, 3D
0.47	0.39	0.67	0.59

Figure 9 visualizes selected relevant modes obtained from the 3D simulation data. We restrict our presentation to the  $u$  and  $v$  velocity components. As expected, the streamwise component of the buffet mode is dominated by the shock motion and the boundary layer separation. Together with the harmonics depicted in the second and third row of figure 9, the buffet mode consist of flow structures that move back and forth (shock region) and up and down (boundary layer) while also pulsating. The shock region of the first three modes depicted below looks very similar to that reported in [13]. However, the modes reported here show clearer dynamics in the boundary layer and the wake, which we suspect is thanks to the volume-weighted state vector. The  $v$  component is similarly dominated by the transonic buffet dynamics related to the shock motion and the flow pulsating separation. The last row of figure 9 shows the 880 Hz mode, which is clearly associated with vortex shedding. Moreover, the fine lamella-like structures below and above the airfoil of the  $u$  component correspond to waves traveling in opposite streamwise direction.

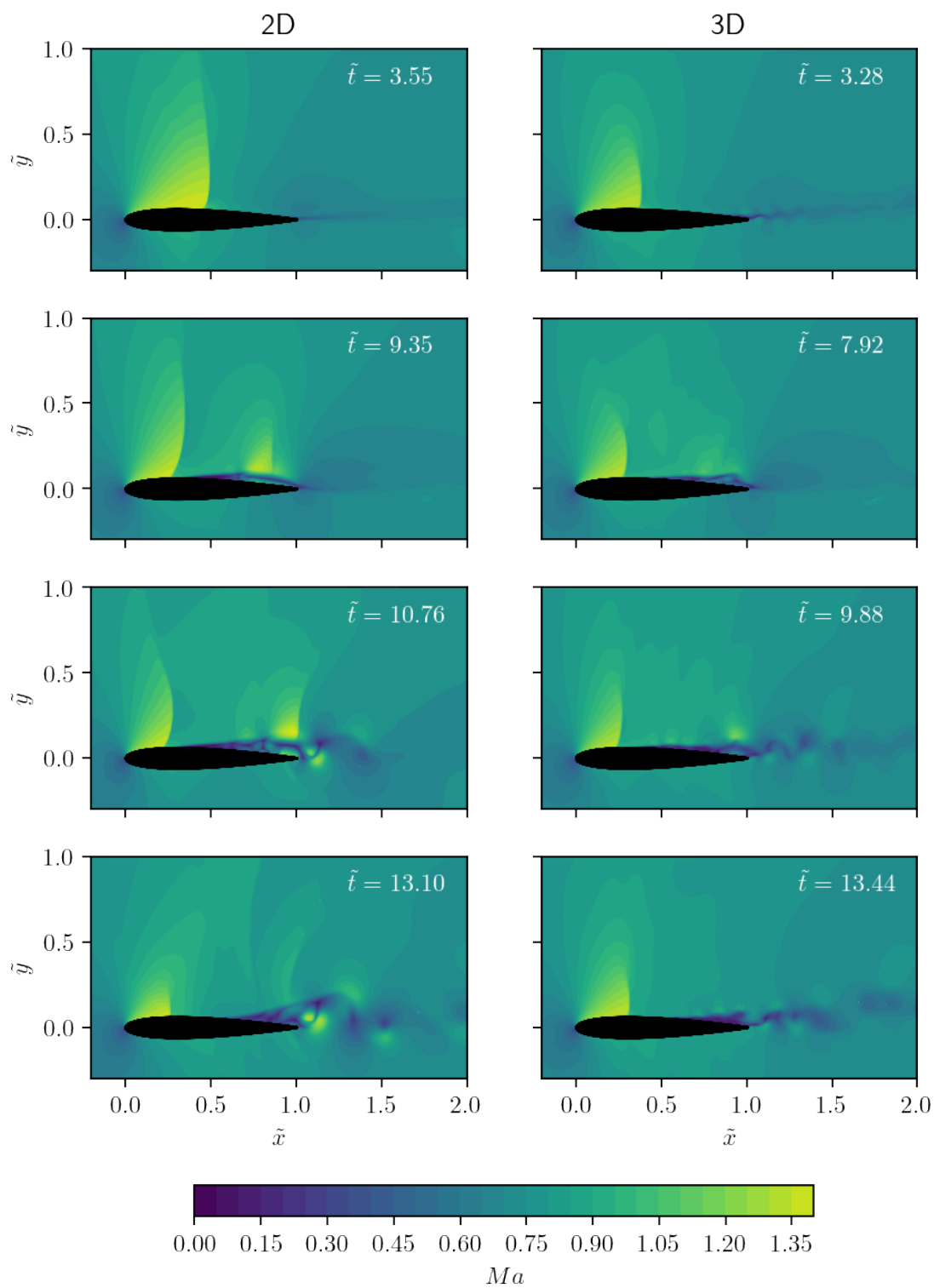


**Fig. 7** Local Mach number field over one buffet cycle in the 2D and 3D simulations; the snapshot times correspond to the markers 1-4 in figure 6.

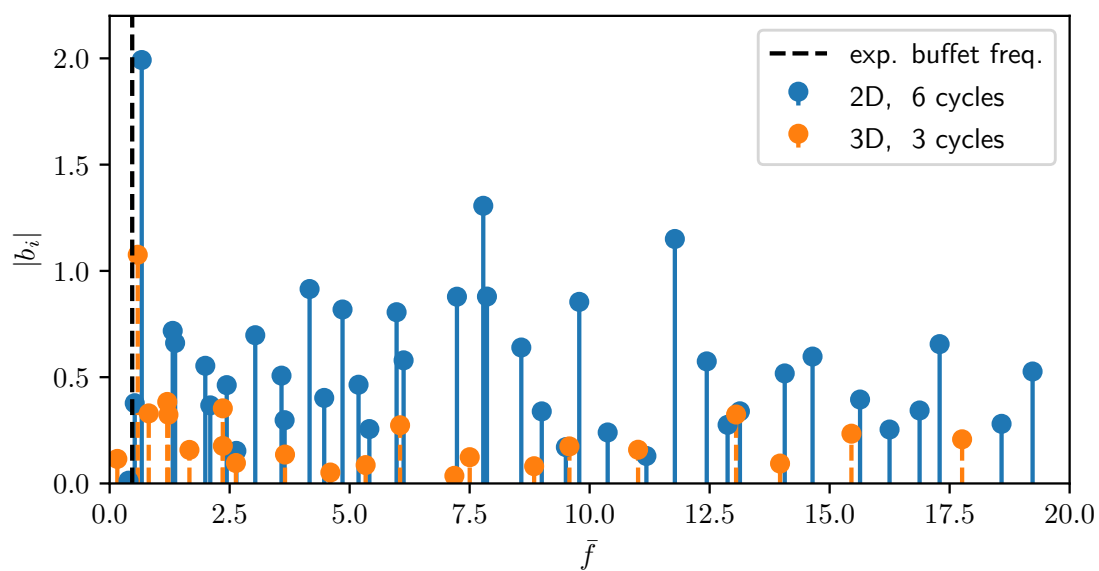


**Fig. 8 DMD spectrum for 2D and 3D simulation data.**

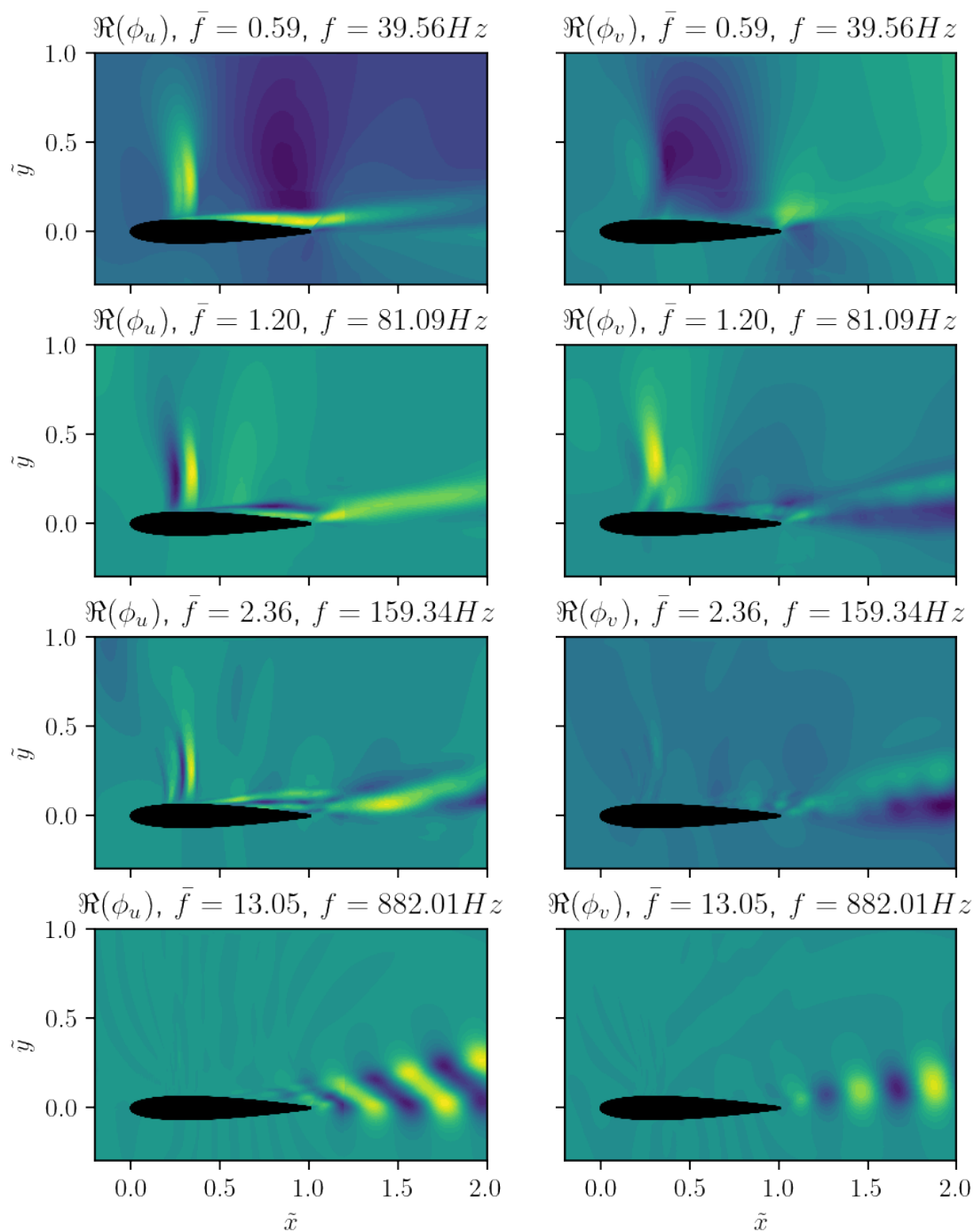


**Fig. 9** DMD modes of 3D simulation data; all fields are normalized to the range [0, 1]; the indices  $u$  and  $v$  indicate the depicted parts of the modes.

## IV. Summary and outlook

In this work, we simulate and analyze 2D and 3D IDDES simulations of a NACA-0012 airfoil under pre- and post-buffet onset conditions. Both simulations yield self-sustained shock-boundary layer interactions at the correct buffet onset angle of attack. The 2D simulations show unphysically strong boundary layer separation close to the trailing edge, which is not present in the 3D simulations. Moreover, the 3D simulations predict the mean shock motion farther upstream than the 2D case and with smaller oscillations. These differences are also reflected in the lift coefficient's mean and fluctuation amplitude, which are  $\approx 38\%$  and  $\approx 8\%$  smaller for the 3D simulation, respectively. Compared to the experiment, the buffet frequency is overestimated by 25% and 45% in the 3D and 2D approaches, respectively. Such discrepancies are not unusual. Nonetheless, we expect the 3D to further approach the experimental values, as more data become available.

The flow dynamics are analyzed using dynamic mode decomposition. Our DMD approach distinguishes itself by employing a well-suitable state vector for compressible flows and by the use of a weighted inner product. DMD identified the buffet mode and two of its harmonics, which exhibit a strong connection between shock, boundary layer, and wake. The method also identified modes associated with vortex shedding at a frequency about 20 times higher than the buffet frequency.

We provide the full simulation setup including all pre- and post-processing tools to enable more consistent results and comparisons in future studies. The flow solver is limited to small Courant numbers, which is why the simulations are time-consuming. Future studies could investigate the application of the implicit OpenFOAM-based HISA solver<sup>†</sup>. Moreover, we only performed mesh dependency studies for the 2D setup. Future investigations could duplicate this analysis for the 3D simulation.

In conclusion, the simulation and analysis of transonic buffets remain a challenging endeavor. Simulation results highly depend on the approach and the employed turbulence closure models. Through the literature survey and our own investigations, we attest that employing URANS simulations that resolves only a small part of the turbulence spectrum or that simplifying the problem to two dimensions yield inconsistent results. Physical results can be robustly achieved with three-dimensional hybrid simulations that capture the necessary physics of transonic buffet.

## Acknowledgments

The authors gratefully acknowledge financial support by the German Research Foundation (DFG) received within the research unit FOR 2895 "Unsteady flow and interaction phenomena at high speed stall conditions". We also acknowledge the illuminating discussions with Steve Brunton and Benjamin Herrmann.

## References

- [1] Giannelis, N. F., Vio, G. A., and Levinski, O., "A review of recent developments in the understanding of transonic shock buffet," *Progress in Aerospace Sciences*, Vol. 92, 2017, pp. 39–84. <https://doi.org/10.1016/j.paerosci.2017.05.004>.
- [2] Brunet, V., *Computational Study of Buffet Phenomenon with Unsteady RANS Equations*, 2003. <https://doi.org/10.2514/6.2003-3679>.
- [3] Deck, S., "Numerical Simulation of Transonic Buffet over a Supercritical Airfoil," *AIAA Journal*, Vol. 43, No. 7, 2005, pp. 1556–1566. <https://doi.org/10.2514/1.9885>.
- [4] Sartor, F., Mettot, C., and Sipp, D., "Stability, Receptivity, and Sensitivity Analyses of Buffeting Transonic Flow over a Profile," *AIAA Journal*, Vol. 53, No. 7, 2015, pp. 1980–1993. <https://doi.org/10.2514/1.J053588>.
- [5] Grossi, F., Braza, M., and Hoarau, Y., "Prediction of Transonic Buffet by Delayed Detached-Eddy Simulation," *AIAA Journal*, Vol. 52, No. 10, 2014, pp. 2300–2312. <https://doi.org/10.2514/1.J052873>.
- [6] Huang, J., Xiao, Z., Liu, J., and Fu, S., "Simulation of shock wave buffet and its suppression on an OAT15A supercritical airfoil by IDDES," *Science China Physics, Mechanics, and Astronomy*, Vol. 55, No. 2, 2012, pp. 260–271. <https://doi.org/10.1007/s11433-011-4601-9>.
- [7] Liu, Y., Wang, G., bin Zhu, S., and Ye, Z., *Numerical study of transonic shock buffet instability mechanism*, 2016. <https://doi.org/10.2514/6.2016-4386>.

<sup>†</sup><https://hisa.gitlab.io/>

- [8] Zimmermann, D.-M., Mayer, R., Lutz, T., and Krämer, E., "Impact of Model Parameters of SALSA Turbulence Model on Transonic Buffet Prediction," *AIAA Journal*, Vol. 56, No. 2, 2018, pp. 874–877. <https://doi.org/10.2514/1.J056193>.
- [9] Fukushima, Y., and Kawai, S., "Wall-Modeled Large-Eddy Simulation of Transonic Airfoil Buffet at High Reynolds Number," *AIAA Journal*, Vol. 56, No. 6, 2018, pp. 2372–2388. <https://doi.org/10.2514/1.J056537>.
- [10] Zhao, Y., Dai, Z., Tian, Y., and Xiong, Y., "Flow characteristics around airfoils near transonic buffet onset conditions," *Chinese Journal of Aeronautics*, Vol. 33, No. 5, 2020, pp. 1405–1420. <https://doi.org/10.1016/j.cja.2019.12.022>.
- [11] Goncalves, E., and Houdeville, R., "Turbulence model and numerical scheme assessment for buffet computations," *International Journal for Numerical Methods in Fluids*, Vol. 46, No. 11, 2004, pp. 1127–1152. <https://doi.org/10.1002/flid.777>.
- [12] Iovnovich, M., and Raveh, D. E., "Reynolds-Averaged Navier-Stokes Study of the Shock-Buffet Instability Mechanism," *AIAA Journal*, Vol. 50, No. 4, 2012, pp. 880–890. <https://doi.org/10.2514/1.J051329>.
- [13] Poplingher, L., Raveh, D. E., and Dowell, E. H., "Modal Analysis of Transonic Shock Buffet on 2D Airfoil," *AIAA Journal*, Vol. 57, No. 7, 2019, pp. 2851–2866. <https://doi.org/10.2514/1.J057893>.
- [14] Xiao, Q., Tsai, H. M., and Liu, F., "Numerical Study of Transonic Buffet on a Supercritical Airfoil," *AIAA Journal*, Vol. 44, No. 3, 2006, pp. 620–628. <https://doi.org/10.2514/1.16658>.
- [15] Illy, S., Lutz, T., and Krämer, E., "On the capability of unsteady RANS to predict transonic buffet," *Proceedings of the Third Symposium Simulation of Wing and Nacelle Stall*, 2012, pp. 1–13.
- [16] MeDevitt, J. B., and Okuno, A. F., "Static and dynamic pressure measurements on a NACA 0012 airfoil in the Ames High Reynolds Number Facility," *NASA TR NASA-TP-2485*, 1985.
- [17] "OpenFOAM simulations of transonic shock buffets on a NACA-0012 airfoil," [https://github.com/AndreWeiner/naca0012\\_shock\\_buffet](https://github.com/AndreWeiner/naca0012_shock_buffet), 2021. Accessed: 2021-11-29.
- [18] Schmid, P. J., "Dynamic mode decomposition of numerical and experimental data," *Journal of Fluid Mechanics*, Vol. 656, 2010, p. 5–28. <https://doi.org/10.1017/S0022112010001217>.
- [19] Taira, K., Brunton, S. L., Dawson, S. T. M., Rowley, C. W., Colonius, T., McKeon, B. J., Schmidt, O. T., Gordeyev, S., Theofilis, V., and Ukeiley, L. S., "Modal Analysis of Fluid Flows: An Overview," *AIAA Journal*, Vol. 55, No. 12, 2017, pp. 4013–4041. <https://doi.org/10.2514/1.J056060>.
- [20] Greenshields, C. J., Weller, H. G., Gasparini, L., and Reese, J. M., "Implementation of semi-discrete, non-staggered central schemes in a colocated, polyhedral, finite volume framework, for high-speed viscous flows," *International Journal for Numerical Methods in Fluids*, Vol. 63, No. 1, 2010, pp. 1–21. <https://doi.org/10.1002/flid.2069>.
- [21] Kurganov, A., Noelle, S., and Petrova, G., "Semidiscrete Central-Upwind Schemes for Hyperbolic Conservation Laws and Hamilton–Jacobi Equations," *SIAM Journal on Scientific Computing*, Vol. 23, No. 3, 2001, pp. 707–740. <https://doi.org/10.1137/S1064827500373413>.
- [22] van Leer, B., "Towards the ultimate conservative difference scheme. II. Monotonicity and conservation combined in a second-order scheme," *Journal of Computational Physics*, Vol. 14, No. 4, 1974, pp. 361–370. [https://doi.org/10.1016/0021-9991\(74\)90019-9](https://doi.org/10.1016/0021-9991(74)90019-9).
- [23] Gritskevich, M. S., Garbaruk, A., Schütze, J., and Menter, F. R., "Development of DDES and IDDES Formulations for the  $k-\omega$  Shear Stress Transport Model," *Flow, Turbulence and Combustion*, Vol. 88, 2012, pp. 431–449. <https://doi.org/10.1007/s10494-011-9378-4>.
- [24] Kutz, J. N., Brunton, S. L., Brunton, B. W., and Proctor, J. L., *Dynamic Mode Decomposition*, Society for Industrial and Applied Mathematics, Philadelphia, PA, 2016. <https://doi.org/10.1137/1.9781611974508>.
- [25] Tu, J. H., Rowley, C. W., Luchtenburg, D. M., Brunton, S. L., and Kutz, J. N., "On dynamic mode decomposition: Theory and applications," *Journal of Computational Dynamics*, Vol. 1, No. 2, 2014, pp. 391–421. <https://doi.org/10.3934/jcd.2014.1.391>.
- [26] Rowley, C. W., Colonius, T., and Murray, R. M., "Model reduction for compressible flows using POD and Galerkin projection," *Physica D: Nonlinear Phenomena*, Vol. 189, No. 1, 2004, pp. 115–129. <https://doi.org/10.1016/j.physd.2003.03.001>.
- [27] Brunton, S. L., and Kutz, J. N., *Data-Driven Science and Engineering: Machine Learning, Dynamical Systems, and Control*, Cambridge University Press, 2019. <https://doi.org/10.1017/9781108380690>.
- [28] "flowTorch - a Python library for analysis and reduced-order modeling of fluid flows," <https://github.com/AndreWeiner/flowtorch>, 2021. Accessed: 2021-11-29.